Engineering Research
Express

PAPER • OPEN ACCESS

True-time delay and mode-matching in Archimedean spiral silicon photonic waveguides

To cite this article: Ahmad Murad and Alina Karabchevsky 2025 *Eng. Res. Express* **7** 035378

IOP Publishing Eng. Res. Express 7 (2025) 035378 https://doi.org/10.1088/2631-8695/ae0413

Engineering Research Express

OPEN ACCESS

RECEIVED
29 July 2025

REVISED
1 September 2025

ACCEPTED FOR PUBLICATION
5 September 2025

PUBLISHED
17 September 2025

PAPER

True-time delay and mode-matching in Archimedean spiral silicon photonic waveguides

Ahmad Murad and **Alina Karabchevsky***

School of Electrical and Computer Engineering, Ben-Gurion University of the Negev, Beer-Sheva 8410501, Israel

* Author to whom any correspondence should be addressed.

E-mail: alinak@bgu.ac.il

Keywords: true time delay, AI reservoir computing, waveguides, ultra-low-loss, highspeed

Abstract

We report a comprehensive analysis and design optimization of true-time delay (TTD) photonic waveguides using compact Archimedean spiral geometries, with a focus on low-loss silicon nitride (Si_3N_4) and silicon-on-insulator (SOI) platforms. Using a combination of finite element and finite-difference time-domain simulations at 1550 nm, we evaluated the propagation characteristics, mode-matching behavior, and bending losses of various waveguide designs. Our results demonstrate that Si_3N_4 rectangular waveguides exhibit superior performance for long optical paths, achieving minimal radiation and scattering losses, whereas SOI is more suitable for compact integration. We further investigated curvature-engineered bends (Euler, Bézier, and circular) and identified Quartic Bézier bends as optimal for tight-radius, low-loss guiding. By minimizing crosstalk through tailored waveguide gaps and carefully engineered S-bend transitions, we present a scalable low-loss TTD architecture. These findings offer critical insights for integrating ultralow-loss, material-efficient delay lines into photonic circuits for applications in signal processing, LiDAR, phased array antennas, and neuromorphic computing.

1. Introduction

True-time delay (TTD) is a fundamental concept in various disciplines. It is critical for the operation of phased array antennas in microwave photonics, where optical delay units are used to achieve multibeam formation [1], and plays an important role in optical signal processing and communication systems by enabling advanced functionalities, such as parallel reservoir computing and information transfer [2]. The development of integrated photonic platforms has further expanded the applicability of TTD, supporting compact and scalable on-chip solutions [3]. Unlike resonance-based delays, which rely on temporarily trapping light, TTD arises from the physical propagation path, providing precise timing control essential for preserving signal integrity and optimizing high-speed reservoir computing (RC) systems.

Optics is a promising candidate for future computing, particularly in neuromorphic architectures [4]. Researchers have explored the combination of the computational power of RC with the high-speed signal handling of photonics. One approach uses coupled semiconductor optical amplifiers [5], although this requires many nodes and presents technological challenges. The delayed feedback approach provides a simpler alternative: Vandoorne *et al* [6] demonstrated photonic RC for signal processing, Paquot *et al* [7] introduced an optoelectronic implementation, and McDonald *et al* [8] analyzed ultrashort TTD lines for compact designs. Larger *et al* [9] further showed that photonic information processing can exceed conventional Turing architectures, although fiber-based implementations remain bulky and unsuitable for chip-scale integration applications.

Reducing losses is paramount in photonic integrated circuits (PICs) for TTD lines, optical gyroscopes [10], and microwave photonic beamforming [11]. LiDAR requires nanosecond-scale delays (path lengths of tens of centimeters to meters) with minimal excess loss; phased arrays typically demand loss budgets below 3–5 dB; and neuromorphic computing imposes latency constraints of tens of picoseconds with low dispersion. Recent reviews have emphasized the critical role of TTD in next-generation microwave photonic systems [12].

Several waveguide platforms have been investigated to achieve this. SOI technology enables dense photonic integration using compact circuits. Vlasov and McNab [13] reported early SOI strip waveguides with losses of a few dB/cm, whereas Li *et al* [14] later demonstrated ultralow-loss. Xu *et al* [15] further reviewed advances in SOI for microwave photonic signal processing. In comparison, silicon nitride (Si_3N_4) supports much lower loss. Pfeiffer *et al* [16, 17] achieved propagation losses down to sub-0.01 dB/m using a damascene reflow process, Zhang *et al* [18] showed sidewall smoothing further suppresses scattering, and Li *et al* [19] developed broadband spiral delay lines with propagation losses of ∼0.02 dB/cm. Romero-García *et al* [20] also demonstrated low-loss integrated delay lines, and Zhang *et al* [21] highlighted progress toward scalable, foundry-compatible Si_3N_4 platforms Complementary designs for digitally tunable delay lines have also been reported [22].

Silica-based waveguides are also strong candidates. Zhang *et al* [23] demonstrated serpentine trapezoidal silica-on-silicon waveguides exceeding 27m with losses as low as 0.05 dB/m, illustrating their potential for ultra-long, low-loss delays. Other architectures include plasmonic spirals for optical trapping [24] and whispering-gallery spirals with compact footprints [25]. Compact spiral Si_3N_4 devices have also been realized, including broadband spirals (∼68cm, excess loss < 0.08 dB) [19] and digitally tunable spirals (10–310 ps delay, < 0.013 dB/ps loss) [22]. Geometry is equally important: Zhang [26], Yi [27], Sun [28], and Bahadori [29] all proposed bend-optimized designs to minimize propagation loss.

Considering the need for ∼40 m-long TTD lines with manageable fabrication complexity, rectangular Si_3N_4 waveguides are an optimal choice for long-path, low-loss applications. Although trapezoidal silica achieves ultralow loss, it is more fabrication-intensive, whereas SOI provides a compact footprint but suffers higher long-path losses.

In this study, we evaluated Archimedean spiral silicon photonic waveguides for TTD applications. Spiral geometries enable compact and efficient delay lines with tunable delay times controlled by spiral parameters. Using finite element and finite-difference time-domain simulations, we analyze the propagation characteristics, loss mechanisms, and delay performance, comparing spiral and linear delay lines. We also investigated curvature-engineered bends to identify designs that minimize losses across different radii. The results provide insight into designing efficient, compact TTD systems for LiDAR, phased arrays, and neuromorphic photonics.

2. Archimedean spirals

Archimedean spirals are frequently used in on-chip designs for long bend waveguides because they efficiently use space and enable smooth transitions between straight waveguides and bends [24]. These designs typically consist of two interwoven spirals: one spiral directs light from the outer edge toward the center, while the other guides it back outward [25]. The spirals can be mathematically represented using the angle θ in Cartesian coordinates as follows:

$$x_c(\theta) = (R_0 + A\theta)\sin(\theta),\\ y_c(\theta) = (R_0 + A\theta)\cos(\theta) \tag{1}$$

Here, the parameter R_0 specifies the initial radius of the spiral, and A determines the spacing between successive loops. Because this function defines only one central curve, two additional parallel curves, ($x_{\text{in}}, y_{\text{in}}$) and ($x_{\text{out}}, y_{\text{out}}$), are introduced as follows: To fully define the waveguide boundaries, the inner and outer edges are represented as follows:

$$x_{\text{in}}(\theta) = x_c(\theta) - n_x(\theta)w_{\text{in}}(\theta),\\ y_{\text{in}}(\theta) = y_c(\theta) - n_y(\theta)w_{\text{in}}(\theta) \tag{2}$$

$$x_{\text{out}}(\theta) = x_c(\theta) + n_x(\theta)w_{\text{out}}(\theta),\\ y_{\text{out}}(\theta) = y_c(\theta) + n_y(\theta)w_{\text{out}}(\theta) \tag{3}$$

where ($n_x(\theta), n_y(\theta)$) define the normal vector of the curve in equation (1) and $w(\theta) = w_{\text{in}}(\theta) + w_{\text{out}}(\theta)$ $w(\theta)$ specifies the width of the waveguide.

The width typically remains constant for the Archimedean portion of a spiral waveguide, excluding the S-bend sections. This section is defined by three main parameters: the initial size of the spiral R_0, waveguide width w, and gap g between adjacent waveguides. The parameters w and g together determine A in the Archimedean spiral by the formula $A = (w + g)/\pi$. Figure 1 illustrates an Archimedean spiral.

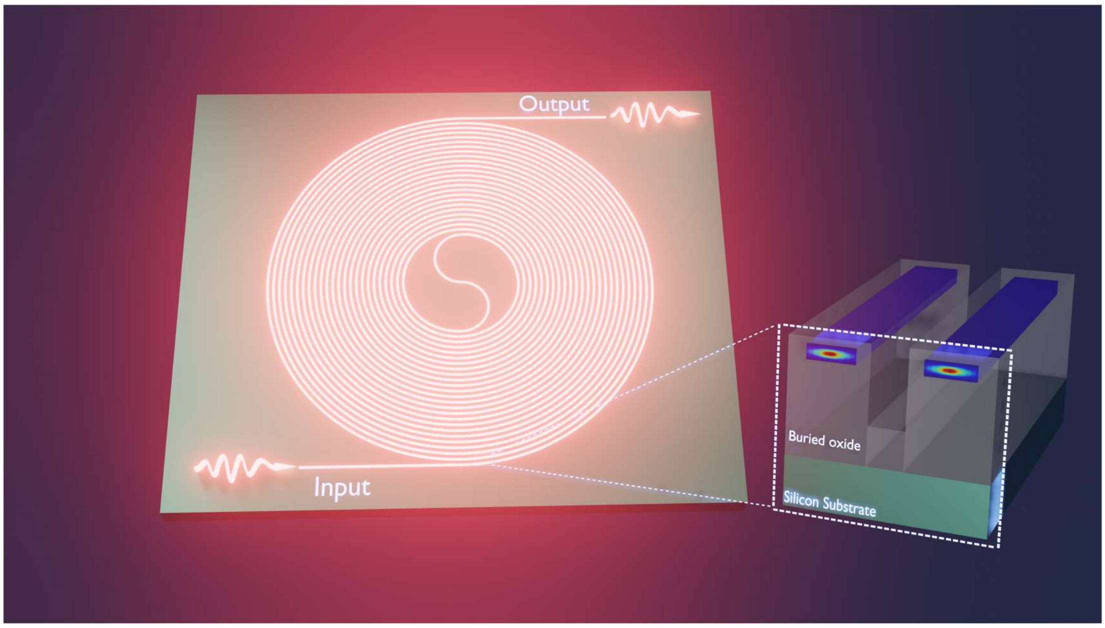

Figure 1. Artistic representation of Archimedean spiral 3D diagram featuring input and output of long-path waveguide.

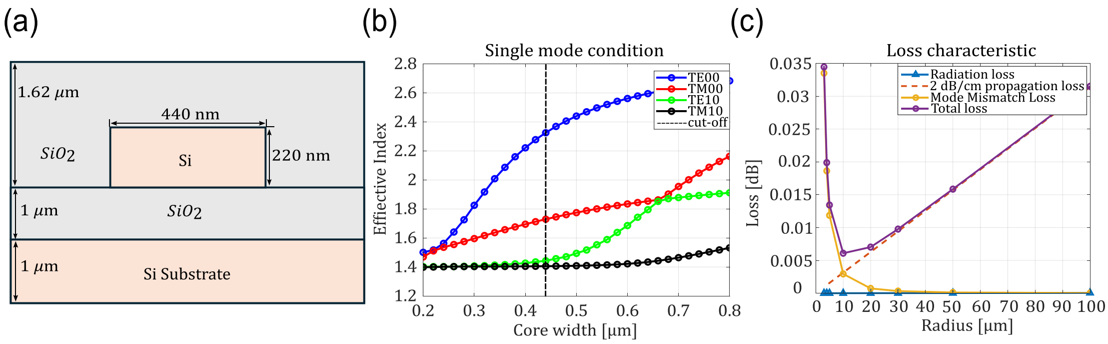

Figure 2. (a) Cross-sectional view schematics of silicon-on-insulator (SOI) platform ridge waveguide (b) Calculated effective index versus core width (c) Calculated loss as a function of spiral radius. The triangular points represent radiation losses, the orange dashed line indicates propagation loss, the yellow open circles show modal mismatch loss, and the purple circular line represents the total loss.

3. Waveguide design

3.1. Silicon on insulator

The most commonly used material platform in silicon photonics is known as 'silicon-on-insulator'(SOI), which is also widely applied in the electronics industry for high-performance circuits and devices. Our design utilizes a 1 μm silicon substrate, a 2.62 μm silicon dioxide (SiO_2) cladding layer, and a 220 nm crystalline silicon core, as illustrated in figure 2(a) [30]. The 220nm core thickness has become a standard, particularly among multiproject wafer foundries and foundry service providers such as imec, LETI, and IME. However, the ideal thickness can vary based on specific applications, and a thickness of 220 nm may not always be optimal. Additionally, variations in the top silicon thickness, which can differ by up to 5 nm, are key parameters to consider [30].

To determine the single-mode condition, we varied the width of the waveguide from 200 to 800 nm, as shown in figure 2(b). A Finite-Difference Eigenmode (FDE) solver was used for comprehensive 2D mode calculations to identify the single-mode condition for the waveguide. The effective indices of the modes are plotted in figure 2(b) for a wavelength of 1550 nm. To achieve a single TE-like mode polarization at 1550 nm, a strip waveguide with a height of 220 nm and a width of 440 nm is required. Under these conditions, the waveguide supports one TE-like and one TM-like mode. An additional TE-like mode appears for waveguides with larger widths, and once the width exceeds 660 nm, a second TM-like mode appears.

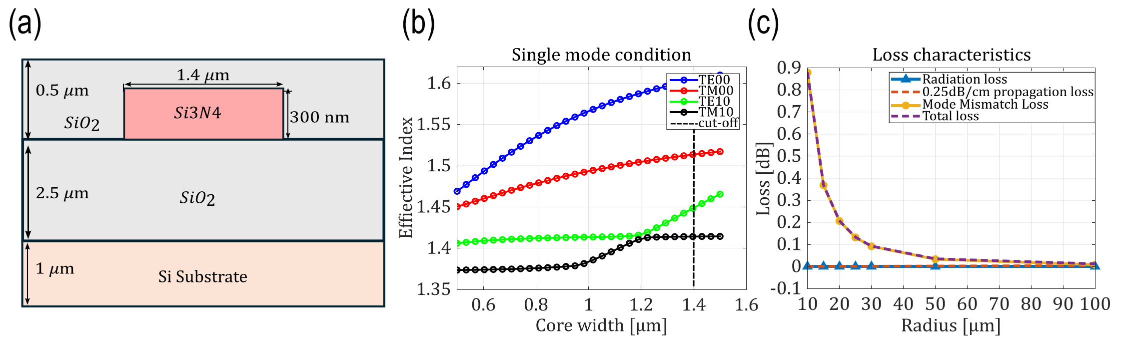

Figure 3. (a) Schematic cross-section of a rectangular Si_3N_4 waveguide. (b) The effective refractive index was simulated as a function of the waveguide width. (c) Loss analysis: triangular markers represent radiation loss, the orange dashed line indicates propagation loss, circular markers show mode mismatch loss, and the purple dashed line represents the total loss.

Table 1. Loss components at $\lambda = 1550$ nm extracted from figures 2(c) and 3(c). Rad.: radiation loss; Prop.: propagation loss; MM: mode mismatch loss; Min R: minimum bend radius for low-loss operation.

Platform	Rad. [dB/90°]	Prop. [dB/cm]	MM [dB/90°]	Total [dB/90°]	Min R [μm]
SOI	~0.08	2.0	~0.15	~0.23	3
Si_3N_4	~0.02	0.25	~0.04	~0.06	10

3.2. Silicon nitride waveguide

In silicon photonic integrated circuits, a rectangular optical waveguide is a basic component, and a single-mode waveguide is commonly used to avoid intermode interference and mode dispersion. To guarantee the single-mode condition of the Si_3N_4 rectangular waveguide, we simulated the modal properties of the Si_3N_4 waveguide using the finite-difference eigenmode (FDE) solver in Lumerical's Mode Solution software. The structure is illustrated in figure 3(a), where the cladding layer has a thickness of 3 μm, the core layer has a thickness of 0.3 μm, and the upper cladding layer has a thickness of 0.5 μm.

To identify the single-mode condition, we analyzed the width of the silicon nitride waveguide at a wavelength of 1550 nm. The relationship between the waveguide width and effective refractive index n_{eff} is shown in figure 3(b). Based on the orange dashed line in the figure, the maximum width for maintaining single-mode operation is 1.4 μm.

3.3. Comparison SOI and Si_3N_4 waveguides

We compared the losses of two waveguide designs: SOI and Si_3N_4. For SOI waveguides, mode calculations for bent waveguides with radii smaller than 3 μm are numerically challenging. The results of the mode power coupling calculations are shown in figure 2(c). For buried SOI waveguides, mode mismatch losses are the dominant source of bend loss, but radiation losses become significant for bend radii below 4 μm. This graph includes a line for the optical scattering losses (propagation loss), assuming 2 dB/cm. We observed that the total loss increased starting from 10 μm.

In contrast, for Si_3N_4 waveguides, scattering losses as low as 0.25 dB/cm have been demonstrated in the literature, which is significantly lower than those for SOI waveguides. This leads to a significantly smaller total loss, particularly over long paths. The results of the mode power coupling calculations are presented in figure 3(c). Mode calculations for Si_3N_4 bent waveguides become challenging below 10 μm radius, compared to 3 μm for SOI. Therefore, SOI waveguides are more attractive for compact layouts, whereas Si_3N_4 is preferable for long-delay, low-loss applications, such as the Archimedean spiral considered here.

To summarize the trade-offs, table 1 lists the key bend and propagation loss components extracted from figures 2(c) and 3(c). Here, 'Rad.' denotes the radiation loss, 'Prop.' denotes the propagation loss, and 'MM' denotes the mode mismatch loss.

From table 1, it is evident that the Si_3N_4 platform offers a significantly lower total bend-related loss compared to SOI for long-delay applications, albeit with a larger minimum bend radius. SOI, while exhibiting higher bend and propagation losses, maintains a much more compact footprint and may still be preferable for shorter delay or highly integrated systems.

3.4. Bent waveguides

Losses due to sidewall roughness are determined by the fabrication process. At the same time, the geometry of waveguide bends affects both mode mismatch and radiation losses, which are the primary focus of this study. To investigate these losses, we use a waveguide mode eigensolver to compute the field profile of a bent waveguide. Various mechanisms contribute to bend losses.

3.4.1. Scattering losses and substrate leakage

Losses are minimal for the short bend lengths under consideration. Specifically, these losses remain small for bend radii up to $\leqslant 10\ \mu$m. The scattering loss (α_s), as defined by the analytical model from [31], is given by

$$\alpha_s = \frac{4\sigma^2 h^2}{\beta\left(r + \frac{2}{p}\right)} = \frac{\sigma^2 k_0^2 h}{\beta} \cdot \frac{E_s^2}{\int E^2\, dx} \cdot \Delta n^2 \tag{4}$$

In this equation, σ denotes the interface roughness, t is the waveguide thickness, k_0 is the free-space wave number, β is the modal propagation constant, and Δn is the refractive index difference between the core and cladding. Here, h and p correspond to the transverse propagation constants in the core and cladding, respectively. The model indicates that the loss is directly proportional to the normalized electric field intensity, $E_s^2/\int E^2\ dx$, at the core/cladding interface and to the square of the interface roughness, σ.

3.4.2. Radiative loss

In highly confined waveguides, especially for TE modes in strip waveguides, radiation is typically small. It contributes to rib waveguides for bend radii $\leqslant 5\ \mu$m and TM-polarized modes. The approximation for the bending or radiation loss (α_r) is [32]

$$\alpha_r \propto \left(\frac{\pi}{\gamma^3 R}\right)^{1/2} \left(\frac{\kappa}{V}\right)^2 \exp\left(-\frac{2}{3}\left(\frac{\gamma^3}{\beta_g^2}\right) R\right) \tag{5}$$

where R is the bend radius, β_g is the propagation constant of the waveguide, and V is proportional to the effective refractive index contrast between the core and cladding. κ is proportional to the refractive index of the waveguide, the free space propagation constant, and β_g, and γ is proportional to the refractive index of the cladding layer, the free space propagation constant, and β_g.

3.4.3. Mode mismatch loss

Mode mismatch loss is the primary contributor to bend-induced losses in photonic waveguides. This results from imperfect mode overlap between the straight and curved sections of the waveguide, leading to scattering at the abrupt transition points at the beginning and end of a fixed-radius bend. Several strategies have been proposed to mitigate the mode-mismatch loss. (a) Laterally offsetting the straight waveguide relative to the bent waveguide to improve the mode overlap [13]. (b) Varying the curvature continuously rather than abruptly. For instance, a 90° bend with an effective radius of 20 μm can be designed with a gradual change in curvature from 0 to $1/15\ \mu\text{m}^{-1}$, and back to 0 [14].

We used Lumerical to calculate the overlap mismatch losses between the modes in the straight and bent sections of the waveguide. First, we calculated the modes for the straight waveguide, then for the bent waveguide, and finally, we performed mode-overlap calculations between the two to determine the power coupling. The overlap measures the fraction of overlapping electromagnetic fields between the two field profiles (modes). The formula is as follows [33].

$$\text{Overlap} = \left| \text{Re}\left[\frac{\left(\int \mathbf{E}_1 \times \mathbf{H}_2^* \cdot d\mathbf{s}\right)\left(\int \mathbf{E}_2 \times \mathbf{H}_1^* \cdot d\mathbf{s}\right)}{\left(\int \mathbf{E}_1 \times \mathbf{H}_1^* \cdot d\mathbf{s}\right)}\right] \cdot \frac{1}{\text{Re}\left(\int \mathbf{E}_2 \times \mathbf{H}_2^* \cdot d\mathbf{s}\right)} \right| \tag{6}$$

3.5. Curvature

Curvature is an important characteristic of a curve and deserves formal definition. Essentially, curvature measures the extent to which a curve bends away from a straight path at any point. It is greater in regions where the curve twists, oscillates, or changes direction sharply and smaller in regions where it approaches a straight line. In addition, assigning a direction to the curvature by defining it as a vector provides further insight. Classical treatments of curvature can be found in differential geometry, as described by do Carmo [34] and Salomon [35]. Recently, Zhang *et al* [26] demonstrated the impact of curvature design on low-loss, n-adjustable bends for photonic integrated circuits. Yi *et al* [27] introduced optimal Bézier curve transitions for ultracompact S-bends, while Sun and Xia [28] developed modified Bézier bend waveguides to further minimize propagation losses. For parametric curves, curvature can be calculated using the following equation:

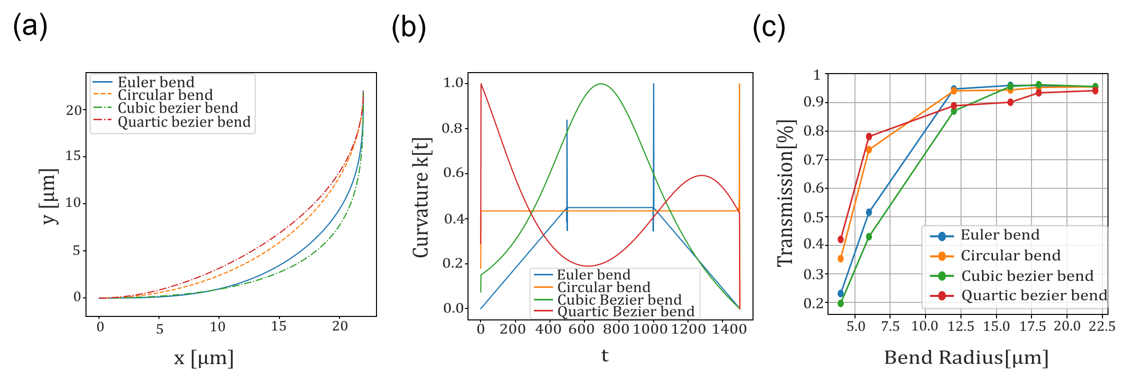

Figure 4. Comparison of three basic bends(a) Schematic of 90° bends composed of a circular bend, an Euler bend, and Bézier bends (b) The relationship between bend curvature K and point index.

$$k(t) = \frac{|x'(t)y''(t) - x''(t)y'(t)|}{(x'(t)^2 + y'(t)^2)^{3/2}}. \tag{7}$$

where $x'(t)$ and $y'(t)$ are the first derivatives of the x and y coordinates with respect to the parameter t, and $x''(t)$ and $y''(t)$ are the second derivatives.

The most popular design approach uses unique bent shapes to decrease the mode mismatch losses by varying the curvature. Such designs include the use of Bézier bends [28], Euler bends, adiabatic bends, circular bends, and low-loss bends based on other special functions [29]. Recent work on bent asymmetric coupled Si_3N_4 waveguides with partial Euler bends has demonstrated further suppression of radiation loss in tight-curvature designs [36].

The **Cubic Bézier** curve is defined by four control points: P_0 at (0, 0), P_1 at (R_{eff}, 0), P_2 at $\left(R_{\text{eff}}, R_{\text{eff}} \cdot \left(1 - \frac{4}{3} \cdot (\sqrt{2} - 1)\right)\right)$, and P_3 at (R_{eff}, R_{eff}). The curve is parameterized by t, ranging from 0 to 1, and is computed using

$$B(t) = (1 - t)^3 P_0 + 3(1 - t)^2 t P_1 + 3(1 - t) t^2 P_2 + t^3 P_3 \tag{8}$$

This curve provides a smooth transition that can effectively minimize the mode mismatch losses. For improved performance in tighter bends, the **Quartic Bézier** curve is defined by five control points and is computed as

$$B_4(t) = (1 - t)^4 P_0 + 4(1 - t)^3 t P_1 + 6(1 - t)^2 t^2 P_2 + 4(1 - t) t^3 P_3 + t^4 P_4 \tag{9}$$

This offers an even smoother curvature, reducing optical losses in small-radius bends. The **Euler** bend, or clothoid curve, features a linearly varying curvature. It is defined by:

$$x = A \int_0^{L/A} \cos\left(\frac{\theta^2}{2}\right) d\theta, \quad y = A \int_0^{L/A} \sin\left(\frac{\theta^2}{2}\right) d\theta \tag{10}$$

where A is the clothoid parameter, L is the curve length, and the relation $R \cdot L = A^2$ defines curvature. The **Euler** bend connects two clothoid curves with a circular arc, thereby ensuring a smooth curvature transition. The **circular** bend is defined by a constant curvature, described as

$$x = R_{\text{eff}} \cos(\theta), \quad y = R_{\text{eff}} \sin(\theta) \tag{11}$$

where R_{eff} is the bending radius and θ ranges from 0 to $\pi/2$.

Figure 4(a) visually compares the geometries of the four types of bends: Euler, circular, cubic Bézier, and quartic Bézier. These geometries are critical in photonic waveguide design, where smooth transitions can significantly reduce the bend and mismatch losses. The comparison in figure 4(b) highlights the curvature profiles of these bends, providing insights into the smoothness of the transition from a straight to a curved segment.

The Euler bend, characterized by an initial Clothoid curve, exhibited a gradual increase in curvature over the first 500 points. This smooth transition helps to minimize abrupt changes. However, a curvature spike occurs at approximately the 500th point because of the transition to a circular arc, where the curvature becomes constant. Another spike is observed at approximately the 1000th point, indicating the transition from the circular arc to the mirrored Clothoid curve. Despite these spikes, the Euler bend maintains a relatively smooth curvature compared to other geometries.

In contrast, the circular bend has a constant curvature throughout, resulting in a sharp curvature transition. This is most noticeable around the 1500th point, where a spike in the curvature indicates an instantaneous

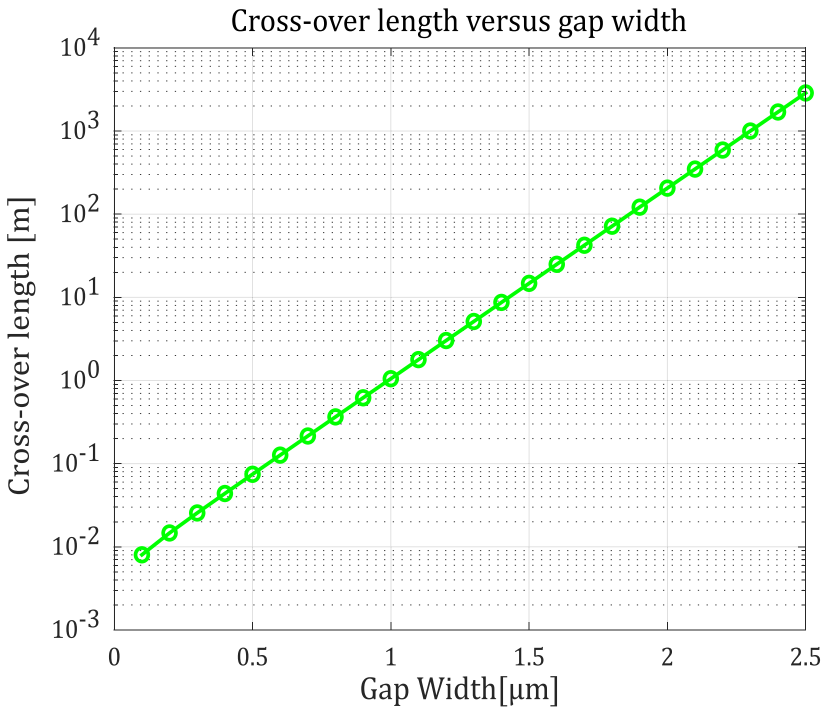

Figure 5. Calculated coupling length L_c as the gap width Wgap in the Archimedean spiral varies.

change in the direction. This sharp transition makes circular bends more prone to losses than smoother bends, such as the Euler bend.

The two Bézier bends (Cubic and Quartic) exhibited distinct curvature behaviors. The cubic Bézier bend has a gradual curvature transition, similar to the Euler bend, but without sharp spikes, making it smoother. However, owing to its more complex curvature profile, the quartic Bézier bend features smoother transitions at smaller radii, offering the most gradual change in curvature. This smoothness is reflected in the minimal spikes, suggesting that the quartic Bézier curve provides the best performance for tight bends.

In figure. In 4(c), we compare the transmission as a function of the bend radius for the four waveguide geometries. As expected, the transmission increased with larger bend radii for all the bends. However, the Quartic Bézier bend shows the highest transmission for smaller bend radii (approximately 4 and 8 μm), outperforming the other geometries in tight bends. This result is consistent with the superior curvature smoothness observed in the Quartic Bézier bend, allowing it to maintain high transmission even with sharp bends.

As the radius of the bend increased, the Euler bend demonstrated a higher transmission, surpassing both Bézier bends (cubic and quadratic). With gradual curvature transitions, the Euler bend performs better for larger-radius bends. In contrast, despite its more straightforward design, the circular bend consistently exhibits the lowest transmission across all radii because of its sharp transitions and constant curvature, which induce higher optical losses.

In summary, the quartic Bézier bend is the most effective for tight bends, whereas the Euler bend excels in applications with larger-radius bends. Although the circular bend is straightforward, it remains the least efficient because of its sharp curvature transitions, which result in higher transmission losses.

3.6. Minimizing losses and cross-talks

To minimize the footprint of the spiral waveguide while preventing undesired evanescent coupling, the gap between adjacent waveguides must be reduced as much as possible. The coupling length L_c can be calculated using the following equation:

$$L_c = \frac{\lambda}{2(n_{\text{eff,TE}_0} - n_{\text{eff,TE}_1})} \tag{12}$$

Here λ is the wavelength and $n_{\text{eff, TE}_0}$ and $n_{\text{eff, TE}_1}$ are the effective indices of the TE_0 and TE_1 supermodes. Here, the effective indices were calculated using a finite element method (FEM) mode solver. Figure 5 illustrates the calculated coupling length as a function of the width of the gap in the spiral waveguide. Because the waveguide spiral is long, the waveguide gap is chosen as $W_{\text{gap}} = 2.5$ μm, which is sufficient to avoid the crosstalk of the adjacent waveguide.

We simulated a 3D model of a 90-degree bend to observe any leaks into the adjacent waveguide, if they existed. The first model was designed to fill the gap with silicon dioxide as the cladding of the waveguide

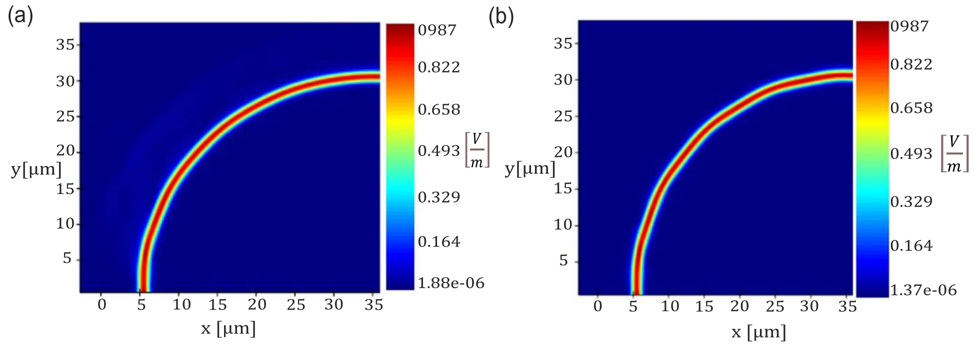

Figure 6. Comparison of two 90-degree bend waveguides with different materials in the gap between two adjacent waveguides. (a) 90-degree bend waveguide with silicon dioxide filling the gap between adjacent waveguides, (b) 90-degree bend waveguide with air filling the gap between adjacent waveguides.

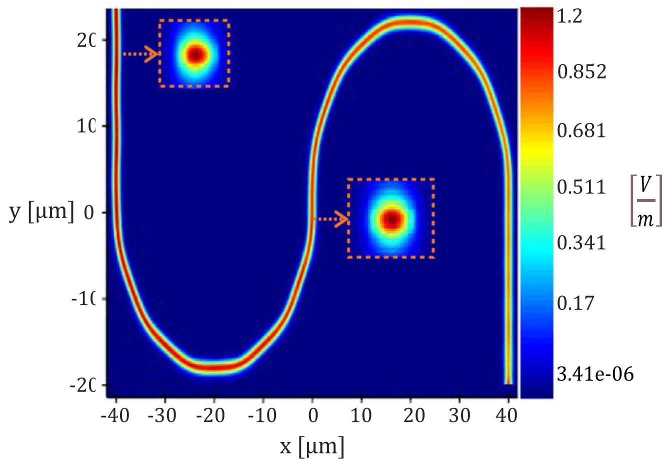

Figure 7. Mode profile S-bend waveguide.

structure, whereas the second model had the gap filled with air. The simulations revealed that when the gap was filled with silicon dioxide, significant light leakage occurred into the adjacent waveguide. In contrast, using air as the cladding effectively suppressed this leakage, as shown in figure 6.

The S-bend in the middle is one of the keys to the waveguide spiral design because the bending radii are abrupt from R to $-R$. To guarantee ultralow bending losses and negligible higher-order mode excitation, we simulated the s-bend waveguide using FDTD simulations, as shown in figure 7. FDTD simulations of the initial 180° S-bends indicated a transmission efficiency of approximately 93%.

3.7. End-to-end transmission of the full Archimedean spiral

A full-vector simulation of the complete two-arm Archimedean spiral at $\lambda = 1550$ nm is computationally prohibitive. Instead, we estimated the end-to-end transmission using a segmented-loss integration that accumulated per-unit-length losses along the spiral centerline and added discrete transition losses. This approach is standard in large-scale PIC link budgets and is consistent with our section-level FEM/FDTD extractions and analytical bend/scattering models [31, 32].

Geometry and length. We used the centerline parameterization already adopted in figure 1:

$$x_c(\theta) = (R_0 + A\theta)\sin\theta,$$
$$y_c(\theta) = (R_0 + A\theta)\cos\theta. \tag{13}$$

Here, R_0 is the inner radius, and $A = (w + g)/\pi$ is set by the waveguide width w and gap g. The differential arc length is

$$d\ell = \sqrt{\left(\frac{dx_c}{d\theta}\right)^2 + \left(\frac{dy_c}{d\theta}\right)^2}\, d\theta = \sqrt{(R_0 + A\theta)^2 + A^2}\, d\theta, \tag{14}$$

and the centerline length from θ_{in} to θ_{out} is

$$L(\theta_{\text{in}}, \theta_{\text{out}}) = \frac{1}{2A}(u\sqrt{u^2 + A^2} + A^2 \ln[u + \sqrt{u^2 + A^2}])\,|_{u=R_0+A\theta_{\text{in}}}^{u=R_0+A\theta_{\text{out}}}. \tag{15}$$

For two interwoven spirals (inward and outward) traversing the same span,

$$L_{\text{spiral}} \approx 2\,L(\theta_{\text{in}}, \theta_{\text{out}}) + L_{\text{S-bends}} + L_{\text{leads}}, \tag{16}$$

with $\theta_{\text{out}} = (R_{\text{out}} - R_0)/A$ and $\theta_{\text{in}} = 0$.

Loss decomposition. We express the total end-to-end loss (in dB) as

$$\mathcal{L}_{\text{tot}}^{(\text{dB})} = \underbrace{\int_0^{L_{\text{spiral}}} \alpha_{\text{p}}^{(\text{dB/m})}\, d\ell}_{\text{propagation}} + \underbrace{\int_0^{L_{\text{spiral}}} \alpha_{\text{b}}^{(\text{dB/m})}(R(\ell))\, d\ell}_{\text{bend radiation}} + \underbrace{\sum_k \mathcal{L}_{\text{tr},k}^{(\text{dB})}}_{\text{transitions/couplers}}, \tag{17}$$

where $\alpha_{\text{p}}^{(\text{dB/m})}$ is the straight-waveguide propagation loss (background + sidewall scattering), $\alpha_{\text{b}}^{(\text{dB/m})}(R)$ is the radius-dependent bend-loss density, and $\mathcal{L}_{\text{tr},k}^{(\text{dB})}$ covers discrete penalties (S-bends, straight↔bend transitions, I/O coupling).

Propagation term. Take $\alpha_{\text{p}}^{(\text{dB/m})}$ from your straight-section simulations for the chosen platform (e.g., Si_3N_4 as in figure 3(c)); its contribution is $\alpha_{\text{p}}^{(\text{dB/m})}\, L_{\text{spiral}}$.

Bend-radiation term. From bend sweeps, use the loss per 90° turn, $\mathcal{L}_{90}^{(\text{dB})}(R)$, and convert to a per-length density via

$$\alpha_{\text{b}}^{(\text{dB/m})}(R) = \frac{\mathcal{L}_{90}^{(\text{dB})}(R)}{(\pi/2)\, R}, \tag{18}$$

Then, $\alpha_{\text{b}}(R)$ is interpolated over the radii realized in the spiral. This is consistent with the expected R-scaling in [32].

Transitions. Add the discrete losses you have already analyzed: two S-bends (cf figure 7), straight↔bend mode mismatch, and I/O coupling. If sidewall scattering was treated separately via [31], include it explicitly; otherwise, fold it into α_{p}.

Discrete implementation. Discretize $[\theta_{\text{in}}, \theta_{\text{out}}]$ into N samples $\{\theta_i\}$ for each arm. For each sample,

$$\begin{aligned} R_i &= R_0 + A\theta_i, \\ \Delta\ell_i &= \sqrt{R_i^2 + A^2}\, \Delta\theta, \end{aligned} \tag{19}$$

and accumulate

$$\mathcal{L}_{\text{spiral}}^{(\text{dB})} \approx 2\sum_{i=1}^{N}(\alpha_{\text{p}}^{(\text{dB/m})} + \alpha_{\text{b}}^{(\text{dB/m})}(R_i))\Delta\ell_i + \mathcal{L}_{\text{S-bends}}^{(\text{dB})} + \mathcal{L}_{\text{leads}}^{(\text{dB})} + \mathcal{L}_{\text{I/O}}^{(\text{dB})}. \tag{20}$$

A modest $N \sim 10^3$ suffices for long spirals. Using the same w, g (thus A) and the bend-loss curves from figures 2(c) and 3(c) shows the end-to-end spiral transmission without a prohibitively large 3D model.

Reporting. We report L_{spiral} from (16), tabulate the extracted $\alpha_{\text{b}}(R)$ used in (18), and provide the resulting $\mathcal{L}_{\text{spiral}}^{(\text{dB})}$ from (20) for the baseline geometry (same $R_0,\ w,\ g$ used throughout this paper). This directly demonstrates the transmission of an entire Archimedean spiral.

3.8. Fabrication tolerance considerations

Although this study is based on idealized simulations, practical implementations are subject to fabrication-induced variations in waveguide geometry and material properties, which can affect performance. Variations in the waveguide width or thickness alter the effective refractive index, potentially affecting the phase accuracy and mode-matching efficiency. Sidewall roughness increases scattering loss, particularly in tight bends, and refractive index variations from material inhomogeneities can introduce phase errors and crosstalk between adjacent waveguides.

Experimental reports indicate that maintaining width deviations within $\pm$ 10 nm and sidewall roughness below 1 nm RMS is critical for keeping excess loss and crosstalk within acceptable limits. Pfeiffer *et al* [17] demonstrated that optimized sidewall smoothing in Si_3N_4 waveguides can reduce scattering losses to below 0.01 dB/m. Similarly, Bauters *et al* [37] reported that precise dimensional control enables propagation losses below 0.1dB/m in long planar waveguides, whereas Lee *et al* [38] showed that fabrication accuracy is essential for preserving low-loss performance in integrated delay-line structures.

Although a full tolerance analysis is beyond the scope of this study, literature reports highlight the fabrication parameters that are most critical for preserving the low-loss and low-crosstalk performance predicted by our simulations.

4. Conclusion

In this study, we present a detailed performance evaluation of Archimedean spiral waveguides for true-time delay (TTD) applications, emphasizing material choices, bend geometries, and design optimization. Through comprehensive FEM and FDTD simulations at the telecom wavelength of 1550 nm, we demonstrated that silicon nitride (Si_3N_4) rectangular waveguides are highly suitable for long optical delay paths owing to their low propagation and bending losses. In contrast, silicon-on-insulator (SOI) waveguides offer advantages for compact and short-delay implementations but suffer from higher radiation losses over extended paths.

We systematically investigated the impact of bend geometry on transmission efficiency and identified the Quartic Bézier bend as the most effective for tight-radius spirals, whereas the Euler bend performed best at larger radii. Moreover, we demonstrated that the evanescent coupling between adjacent waveguides in compact spirals can be effectively suppressed by optimizing the gap and using air cladding. The S-bend region was optimized to ensure minimal loss and mode distortion.

Overall, this study provides a foundational framework for designing compact, low-loss TTD elements using spiral waveguides in integrated photonics. These insights are directly applicable to next-generation optical systems in RF beamforming, LiDAR, neuromorphic computing, and high-speed signal processing, where precise timing and low-latency performance are essential.

Acknowledgments

We acknowledge the support of Israel Science Foundation (ISF) - #1023/24.

Data availability statement

All data that support the findings of this study are included within the article (and any supplementary files).

Appendix

In our research, we conducted a comprehensive analysis by modeling the optical field profile of the fundamental mode at a wavelength of 1550 nm using COMSOL Multiphysics finite element method analysis. Additionally, the research encompassed simulations in Lumerical with different materials. We investigated three different waveguide geometries: trapezoidal, rectangular, and circular. By examining these waveguide configurations, we aimed to compare their respective optical field profiles and assess the variations in their behavior and characteristics. To ensure a fair comparison among the different waveguide geometries, we ensured that the height of the trapezoidal waveguide remained fixed. To maintain consistency in the total area of the waveguide in all cases, we adjusted the width of the rectangular waveguide. Specifically, the width of the rectangular waveguide was set to the average of the top and bottom widths of the trapezoidal waveguide. This approach allowed us to maintain a uniform total waveguide area and facilitate an accurate comparison of the optical field profiles among the different waveguide geometries. We observed that the electric-field distributions in all three devices, including the trapezoidal waveguide, exhibited symmetry. This symmetry indicates minimal leakage of the optical field into the membrane surface. However, one notable distinction is that the trapezoidal waveguide has a significantly smaller effective mode area than the rectangular and circular waveguides. By presenting these findings, we contribute to the understanding of waveguide behavior and provide insight into the differences between the trapezoidal waveguide and other geometries in terms of the effective mode area. For comparison, we also modeled silica rectangular and circular waveguides with the same width and at the same wavelength. The results at 1550 nm for the TE mode are shown in figures A1(a)–(c) and used to form figure A1(d). The electric field distributions in all three devices were symmetric, indicating minimal leakage into the membrane. However, the effective mode area of the trapezoidal waveguide is significantly smaller than that of the other geometries [23].

Our goal was to simplify the waveguide fabrication process. Because fabricating a trapezoidal waveguide is complex, we chose to use a rectangular waveguide instead.

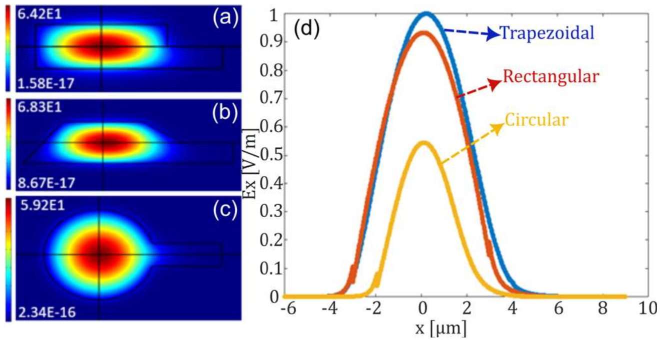

Figure A1. Finite element method simulation of the electric field distribution (TE mode) of (a) trapezoidal, (b) rectangular waveguide, and (c) circular waveguide at 1550 nm. (d) Comparison of the mode profile intensity along the x horizontal direction, normalized to the highest Intensity in the trapezoidal device.

References

[1] Ye X, Zhang F and Pan S 2015 Optical true time delay unit for multi-beamforming *Opt. Express* **23** 10002–8
[2] Karabchevsky A, Katiyi A, Ang A S and Hazan A 2020 On-chip nanophotonics and future challenges *Nanophotonics* **9** 3733–53
[3] Karabchevsky A and Choudhary A 2024 *On-Chip Photonics: Principles, Technology and Applications* (Elsevier)
[4] Caulfield H and Dolev S 2010 Why future supercomputing requires optics *Nat. Photonics* **4** 05
[5] Vandoorne K, Dambre J, Verstraeten D, Schrauwen B and Bienstman P 2011 Parallel reservoir computing using optical amplifiers *IEEE Trans. Neural Netw.* **22** 1469–81
[6] Vandoorne K, Dierckx W, Schrauwen B, Verstraeten D, Baets R, Bienstman P and Campenhout J V 2008 Toward optical signal processing using photonic reservoir computing *Opt. Express* **16** 11182–92
[7] Paquot Y, Duport F, Smerieri A, Dambre J, Schrauwen B, Haelterman M and Massar S 2012 Optoelectronic reservoir computing *Sci. Rep.* **2** 287
[8] McDonald N, Hollingsworth A, Beninati S, Lim C, Ji W, Shi C, Agiorgousis M L, Zhang S and Huang Z R 2020 Analysis of an ultra-short true time delay line optical reservoir computer *J. Lightwave Technol.* **38** 3584–91
[9] Larger L, Soriano M C, Brunner D, Appeltant L, Gutierrez J M, Pesquera L, Mirasso C R and Fischer I 2012 Photonic information processing beyond turing: an optoelectronic implementation of reservoir computing *Opt. Express* **20** 3241–9
[10] Lefevre H C 2022 *The Fiber-optic Gyroscope* (Artech house)
[11] Xue X, Xuan Y, Bao C, Li S, Zheng X, Zhou B, Qi M and Weiner A M 2018 Microcomb-based true-time-delay network for microwave beamforming with arbitrary beam pattern control *J. Lightwave Technol.* **36** 2312–21
[12] Capmany J, Gasulla I and Marpaung D 2023 True-time delay photonic beamforming: state of the art *IEEE J. Sel. Top. Quantum Electron.* **29** 1–18
[13] Vlasov Y A and McNab S J 2004 Losses in single-mode silicon-on-insulator strip waveguides and bends *Opt. Express* **12** 1622–31
[14] Li G *et al* 2012 Ultralow-loss, high-density soi optical waveguide routing for macrochip interconnects *Opt. Express* **20** 12035–9
[15] Xu Y, Li M, Hu T and Yao J 2022 Integrated silicon photonics for microwave photonic signal processing: recent progress *Nanophotonics* **11** 2725–47
[16] Pfeiffer M H P, Zervas M, Fülöp András and Kippenberg T J 2023 Sub-0.01 db/m silicon nitride waveguides enabled by photonic damascene reflow *Nat. Commun.* **14** 1234
[17] Pfeiffer M H P, Kordts A, Brasch V, Zervas M, Geiselmann M, Jost J D and Kippenberg T J 2018 Ultra-smooth silicon nitride waveguides based on the damascene reflow process: fabrication and loss origins *Optica* **5** 884–92
[18] Zhang L, Miller S, Chen X and Lee K 2022 Low-loss silicon nitride photonics through optimized sidewall smoothing techniques *Opt. Lett.* **47** 3945–8
[19] Li X, Zhang Y, Wang H and Chen L 2022 Broadband spiral optical delay on a silicon nitride platform at 1310 nm *Opt. Commun.* **505** 127486
[20] Romero-García S, Mora J, Ortigosa-Blanch A and Capmany J 2021 Low-loss integrated photonic delay lines in Si_3N_4 *APL Photonics* **6** 046104
[21] Zhang H, Chen W, Xu Q and Kippenberg T J 2023 Advances in ultra-low-loss silicon nitride photonics *Optica* **10** 123–34
[22] Zhou M, Sun P, Liu J and Xu Q 2025 Design and simulation of optical waveguide digital adjustable delay lines *Photonics* **12** 679
[23] Zhang X, Harrison M, Harker A and Armani A M 2012 Serpentine low loss trapezoidal silica waveguides on silicon *Opt. Express* **20** 22298–307
[24] Oktafiani F, Chen J-Q and Lee P-T 2022 Ultra-compact archimedes spiral plasmonic lens with a circular groove for low power optical trapping in the far-field region *Opt. Express* **30** 44018–28
[25] Chen T, Lee H and Vahala K J 2014 Design and characterization of whispering-gallery spiral waveguides *Opt. Express* **22** 5196–208
[26] Zhang L *et al* 2023 Low-loss, ultracompact n-adjustable waveguide bends for photonic integrated circuits *Opt. Express* **31** 2792–806
[27] Yi D, Zhang Y and Tsang H K 2021 Optimal bezier curve transition for low-loss ultra-compact s-bends *Opt. Lett.* **46** 876–9
[28] Sun T and Xia M 2022 Low loss modified bezier bend waveguide *Opt. Express* **30** 10293–305
[29] Bahadori M, Nikdast M, Cheng Q and Bergman K 2019 Universal design of waveguide bends in silicon-on-insulator photonics platform *J. Lightwave Technol.* **37** 3044–54
[30] Chrostowski L and Hochberg M 2015 *Silicon Photonics Design: From Devices to Systems* (Cambridge University Press)
[31] v Tien P K 1971 Light waves in thin films and integrated optics *Appl. Opt.* **10** 2395–413
[32] Marcatili E A J 1969 Bends in optical dielectric guides *Bell Syst. Tech. J.* **48** 2103–32
[33] (Ansys) 2024 Overlap script command *Ansys Support Article* Accessed: 2024-08-30
[34] do Carmo M P 1976 *Differential Geometry of Curves and Surfaces* (Prentice-Hall)

[35] Salomon D 2006 *Curves and Surfaces for Computer Graphics* (Springer)
[36] Zhang W, Chen H, Li M and Xu Q 2024 Silicon nitride bent asymmetric coupled waveguides with partial euler bends *Opt. Express* **32** 5678–89
[37] Bauters J F, Heck M J R, John D, Dai D, Tien M-C, Barton J S, Leinse A, Heideman R G, Blumenthal D J and Bowers J E 2011 Planar waveguides with less than 0.1 db/m propagation loss fabricated with wafer bonding *Opt. Express* **19** 24090–101
[38] Lee H, Chen T, Li J, Yang K Y, Jeon S, Painter O and Vahala K 2013 Low-loss si_3n_4 waveguides for optical delay lines and filters *Opt. Express* **21** 17951–9